



Extensional viscosity and thinning of a fiber suspension thread

Joris Château,¹ Élisabeth Guazzelli ,² and Henri Lhuissier ^{1,*}

¹*Aix Marseille Univ, CNRS, IUSTI, Marseille, France*

²*Université de Paris, CNRS, Matière et Systèmes Complexes (MSC), UMR 7057, Paris, France*



(Received 7 September 2020; accepted 29 March 2021; published 21 April 2021)

The extensional effective viscosity, η_e , of a suspension of solid cylindrical fibers in a Newtonian liquid is measured from the gravitational stretching of a quasisteady jet. We vary the length-to-diameter aspect ratio of the fibers, a , from ~ 10 to $\sim 10^2$, and the particle volume fraction, ϕ , in the range $a\phi \sim 0.1$ – 2 . For low values of ϕ , the extensional viscosity is found to agree with Batchelor's model for the dilute regime, which assumes noninteracting fibers aligned with the stretching direction, but for higher concentrations, η_e is found to increase much more strongly with increasing ϕ than predicted by available models assuming purely hydrodynamics interactions between the fibers. Additional experiments are performed on the breakup of an unstable capillary bridge for $a = 11$. Although the variability in the bridge shape and the deviation from a viscous Newtonian dynamics in the late stage of the breakup increase significantly with increasing ϕ , it is found that the mean total duration of the breakup is in good agreement with a Newtonian effective dynamics limited by the extensional viscosity, η_e .

DOI: [10.1103/PhysRevFluids.6.044307](https://doi.org/10.1103/PhysRevFluids.6.044307)

I. INTRODUCTION

The formation, deformation, and fragmentation of elongated structures, such as jets or threads, involve essentially extensional flows, for which the rheological response of the deformed medium may differ strongly from its response to a shear flow, in particular when the medium has a microstructure depending on the type of deformation. A typical example is that of a suspension of elongated particles, such as solid fibers, which, provided they are diluted enough, align with the straining direction in a purely extensional flow, while they tumble in a pure shear.

For fibers that are rigid, non-Brownian, suspended in a Newtonian liquid having a viscosity η_0 , and sufficiently small to neglect inertial effects, the bulk response of the suspension is pseudo-Newtonian in all flows, in the sense that all the bulk effective stresses (except the undetermined bulk pressure) must be proportional to both η_0 and the actual deformation rate. Moreover, if the orientation of the particles has statistically the same symmetry as the bulk flow, the deviatoric part of the bulk stresses must have the same tensorial form as for a Newtonian liquid. Importantly, this condition is verified for a liquid thread containing fibers with an initially random orientation or for a jet extruded from a cylindrical nozzle that are both stretched parallel to their own axis, since the fibers are expected to evolve from the initial isotropic or partly aligned configuration to the final aligned state while preserving the axial symmetry of the flow. In this case, the extensional bulk rheology is fully defined by a single coefficient, the extensional effective viscosity $\eta_e \equiv \tau_{ij}/2E_{ij}$, where \mathbf{E} and $\boldsymbol{\tau}$ are the strain rate tensor and the deviatoric part of the viscous stress tensor, respectively. Note that from this definition, η_e is equal to the shear viscosity, η_s , in the case of a Newtonian liquid.

*henri.lhuissier@univ-amu.fr

In the absence of contact between the fibers, η_e can only result from hydrodynamic perturbations of the mean flow by the fibers, and the fibers can only interact via hydrodynamic forces. In the case of rigid particles, the effective viscosity depends only on the particle volume fraction, ϕ , the length-to-diameter aspect ratio of the fibers, $a = l/d$, and the degree of alignment of the fibers. A series of expressions for η_e have been derived by Batchelor [1] and Shaqfeh and Fredrickson [2] for different degrees of fiber dilution in a uniaxial straining flow ($\mathbf{E} = -\dot{\epsilon}/2\mathbf{e}_x\mathbf{e}_x - \dot{\epsilon}/2\mathbf{e}_y\mathbf{e}_y + \dot{\epsilon}\mathbf{e}_z\mathbf{e}_z$). These authors have considered slender fibers ($a \gg 1$), neglected inertia and frictional contact between the fibers, and assumed simplified hydrodynamic interactions between the fibers. Most models have also considered parallel fibers aligned with the stretching direction (\mathbf{e}_z). In the dilute limit ($a^2\phi/\ln a \ll 1$), i. e., when the mean distance between neighboring fibers, $\sim d/\sqrt{\phi}$, is larger than the hydrodynamic range, $\sim l/\sqrt{\ln a}$, the interaction between the fibers can be neglected and the specific viscosity, $\eta_e/\eta_0 - 1$, is proportional to ϕ . By summing the additional stresses due to force-free, isolated fibers (i. e., stresslets; see [3–5]), Batchelor [1] obtained

$$\frac{\eta_e}{\eta_0} - 1 = \frac{2\varepsilon Q(\varepsilon)}{9} a^2 \phi, \quad \text{with} \quad \varepsilon = \frac{1}{\ln(2a)}, \quad (1)$$

where the shape factor $Q(\varepsilon) = \frac{1+0.64\varepsilon}{1-3\varepsilon/2} + 1.659\varepsilon^2 + O(\varepsilon^3)$ is of order 1 in practice. The alignment of the particles with the direction of the largest strain maximizes the dissipation. Due to the linearity of the stresses, Eq. (1) can be extended to any distribution of particle orientation. For isotropic particles, the specific viscosity is five times as small as that given by Eq. (1). Experiments with a jet stretched with a rotating cylinder [6,7] or by gravity [8] have verified the validity of Eq. (1) for dilute suspensions of thin elongated fibers ($d \lesssim 10 \mu\text{m}$, $a \sim 50\text{--}1200$, and $\phi \sim 5 \times 10^{-4}$ to 0.01). Modifications of Eq. (1) have also been proposed to account for the weak hydrodynamic interactions between the fibers in the so-called semidilute regime where the mean distance between the fibers is smaller than the hydrodynamic range while remaining larger than the fiber diameter ($d \ll d/\sqrt{\phi} \lesssim l/\sqrt{\ln a}$). For semidilute suspensions of aligned fibers, Batchelor [1] and Shaqfeh and Fredrickson [2] have obtained, respectively,

$$\frac{\eta_e}{\eta_0} - 1 = \frac{4}{9} \frac{1}{\ln \pi/\phi} a^2 \phi, \quad (2a)$$

$$\frac{\eta_e}{\eta_0} - 1 = \frac{4}{9} \frac{1}{\ln[\ln(1/\phi)/\phi] + 0.1585} a^2 \phi, \quad (2b)$$

from a cell model approximation with a mean field cell size $d/\sqrt{\phi}$ and a multiple scattering model of the hydrodynamic interactions, respectively.

Beyond these purely hydrodynamic regimes, a different rheological behavior may be expected as ϕ is increased since solid contacts between the particles must become important at some point. Above solid fractions of order $1/a$ [9–11], solid contacts may prevent the fibers from aligning, and even for a given orientation distribution of the particles, an increase in solid contacts between the particles is expected as ϕ becomes of order 1 or as a is sufficiently increased. This should definitely affect the particle flow and hence the overall dissipation. This limit has been documented recently for a pure shear flow [12], but data are not available for straining flow.

These questions are precisely addressed in the present contribution by measuring the extensional effective viscosity of a suspension of solid cylindrical fibers in a Newtonian liquid from the gravitational stretching of a quasisteady jet. These experiments are complemented by additional observations on the breakup of an unstable capillary bridge using the same fiber suspensions. The experimental methods are described in Sec. II, and the results in Sec. III. Conclusions are drawn in Sec. IV.

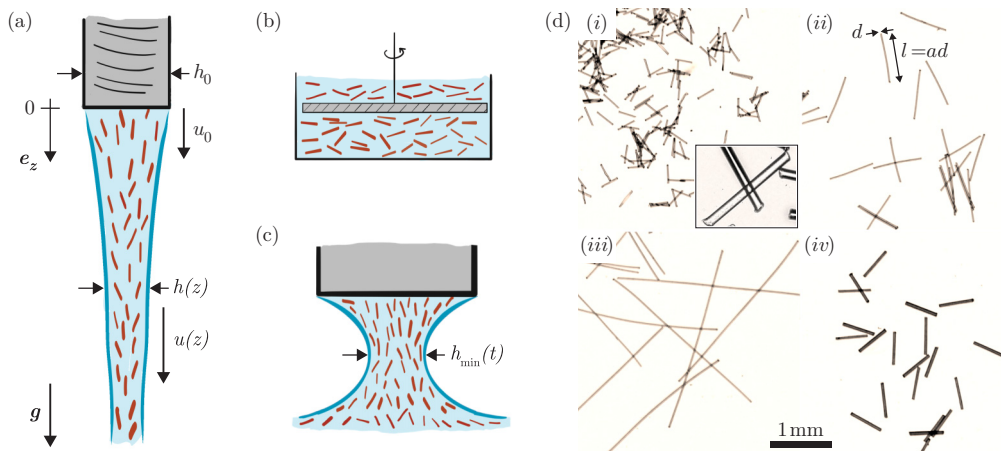


FIG. 1. Setups and fibers. (a) Constant flow rate jet stretched by gravity used for the extensional rheometry. (b) Shear cell used for the shear rheometry. (c) Capillary bridge breakup configuration. (d) Cylindrical polyamide fibers used for the experiments: (i) $d = 28.9 \mu\text{m}$, $a = 10.8$. (ii) $d = 28.3 \mu\text{m}$, $a = 27.6$. (iii) $d = 28.1 \mu\text{m}$, $a = 106$. (iv) $d = 48.1 \mu\text{m}$, $a = 11.5$.

II. MATERIALS AND EXPERIMENTAL METHODS

We use cylindrical polyamide fibers manufactured for flocking applications (provided by the Pinfloc company). Their diameter, d , is varied between $\simeq 28$ and $\simeq 48 \mu\text{m}$, which is much smaller than the diameter of the liquid thread ($h \sim 1\text{--}10 \text{ mm}$) while their length-to-diameter ratio, $a = l/d$, is varied between $\simeq 10$ and $\simeq 100$; see Fig. 1(d) and Table I, which also provides combinations of the relevant parameters. The fiber ends are slightly tapered because of the cutting process by which they are manufactured. They are suspended in a Newtonian liquid having a density matching their own density ($\rho = 1140 \text{ kg/m}^3$) and which wets them well. The liquid is an aqueous solution of PEGPG [3.9 kg/mol poly(ethylene glycol-ran-propylene glycol)-monobutylether by Sigma-Aldrich] or of UCON oil (polyalkylene glycol-composed lubricant UCON 75-H 90 000 by Dow) with ZnCl_2 (zinc chloride; Sigma-Aldrich). Its viscosity, η_0 , is varied between 0.13 and 3.1 Pa s in order to obtain an effective viscosity of the suspension in the range where the measurements on the jet are accurate (see below) and those on the capillary bridge are free of inertial effects (see below). The particle volume fraction, ϕ , is varied between $\sim 10^{-3}$ and 10^{-2} and a value close to the largest volume fraction at which the suspension could be processed without noticeable aeration or self-filtration, i. e., 0.24, 0.07, and 0.02 for $l/d = 11, 28$, and 106, respectively. The suspensions are prepared at the desired volume fraction and poured in a plastic syringe which is connected to the jet or bridge setups. Note that for the highest volume fractions ($\gtrsim 0.2$), clear nonuniformities in the dispersion of the fibers are observed. Apparent clusters of fibers, with a typical dimension of a few fiber lengths, are found to form and to vanish dynamically as the suspension is gently mixed.

TABLE I. Characteristics of the fibers (the \pm symbol indicates the standard deviation over 30 fibers) and concentration ranges of the suspensions.

	$d \text{ } (\mu\text{m})$	$a = l/d$	$\phi/100$	$a\phi$	$a^2\phi$
(i)	28.9 ± 1.2	10.8 ± 1.8	1 – 24	0.108 – 2.59	1.16 – 27.9
(ii)	28.3 ± 0.9	27.6 ± 0.9	0.3 – 7	0.083 – 1.93	2.28 – 53.3
(iii)	28.1 ± 1.3	106 ± 5.5	0.08 – 2	0.085 – 2.12	8.96 – 224
(iv)	48.1 ± 4.2	11.5 ± 1.1	5	0.57	6.61

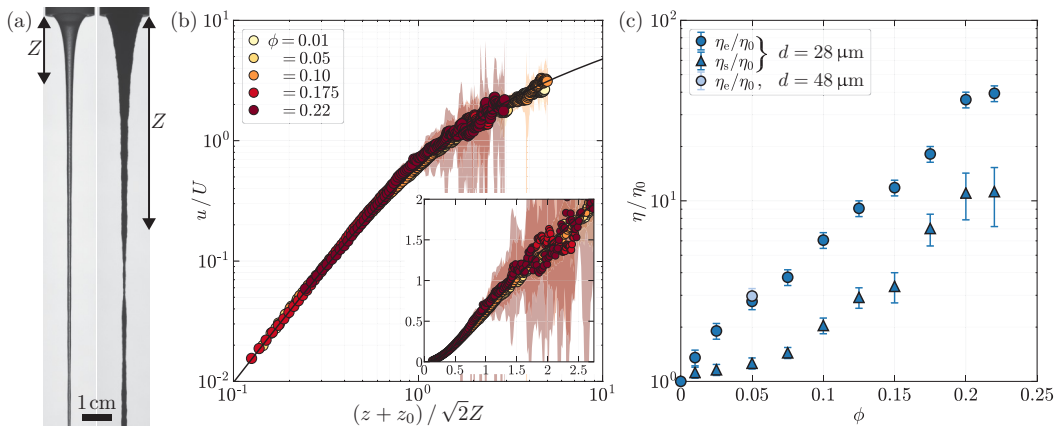


FIG. 2. (a) Typical jets observed for $a \approx 11$ and $d \approx 28 \mu\text{m}$, $\phi = 0.01$ (left, $\eta_0 = 3.1 \text{ Pa s}$) and $\phi = 0.20$ (right, $\eta_0 = 0.66 \text{ Pa s}$), and $u_0 = 1.36 \text{ cm/s}$. (b) Mean velocity versus distance to the nozzle for different volume fractions [same fibers as in (a), $\eta_0 = 3.1 \text{ Pa s}$ for $\phi < 0.10$ and $\eta_0 = 0.66 \text{ Pa s}$ for $\phi \geq 0.10$]. The solid line shows the velocity for a Newtonian liquid, Eq. (4), and z_0 determines the velocity at the nozzle u_0 , i. e., $u(z_0) = u_0$. The shaded envelopes indicate the standard deviation of $u_0 h_0^2 / U h^2$. Inset: Same data in linear scales. (c) Relative effective viscosity of the suspensions as measured from the jet velocity profile (η_e / η_0) and with the shear cell (η_s / η_0).

The jet setup is sketched in Fig. 1(a). It consists in forming a quasisteady jet by extruding a fiber suspension through a vertical nozzle with a constant flow rate and observing the gravitational thinning of the jet. The suspension is extruded through a cylindrical nozzle having an inner diameter $h_0 = 11.6 \text{ mm}$ (and a length $\simeq 30 \text{ mm}$). A constant flow rate with mean velocity at the nozzle $u_0 \sim 1 \text{ cm/s}$ is imposed with the help of a rigid piston and a high-precision translation stage. The thinning of the jet is imaged from a side view using a camera, see Fig. 2(a), and the thickness profile $h(z)$ is obtained by detecting the jet contour. The extensional effective viscosity is obtained with the same procedure as in [13] (also used previously by [8]), by comparing the stretching of the suspension jet with that expected for a Newtonian liquid. The quasisteady velocity profile of the jet, $u(z)$, is obtained from the measurement of the thickness profile $h(z)$, by making use of the constant flow rate assumption, $u(z) = u_0 h_0^2 / h(z)^2$, and averaging over a sufficient time ($\sim 10 \text{ s} \gg h_0 / u_0$). It has been verified that very close values are obtained by measuring directly the velocity from the displacement of the surface corrugations of the jet [13]. The reference Newtonian profile is obtained from the unidimensional, slender-slope approximation of the momentum and mass equations [14],

$$uu_z = g + \frac{3\eta_e}{\rho} \frac{(h^2 u_z)_z}{h^2}, \quad h^2 = \frac{h_0^2 u_0}{u}, \quad (3)$$

which is relevant in the present case of an elongated geometry ($h_z \ll 1$) and negligible surface tension (the Weber number $\rho h_0 U^2 / \sigma$ is of order 20). Introducing the visco-gravity velocity scale, $U = (3\eta_e g / \rho)^{1/3}$, which determines whether the fall of the jet is limited by viscous stretching ($u \ll U$) or is free ($u \gg U$), and the visco-gravity length scale, $Z = (9\eta_e^2 / \rho^2 g)^{1/3}$, which represents the typical distance from the nozzle at which U is reached for a slow extrusion ($u_0 \ll U$), these equations can be combined into [15]

$$\left(\frac{u}{U}\right)' = \frac{U}{u} + \left(\frac{(u/U)'}{u/U}\right)', \quad (4)$$

where $'$ denotes $Z \partial_z$. For a sufficiently long jet ($z \gg Z$), Eq. (4) [with $u(0) = 0$ and $u'(\infty)/U = 0$] determines a single universal velocity profile $u(z)$, whose scales, U and Z , embed the extensional

effective viscosity of the jet, $\eta_e = \rho U^3 / 3g = \rho \sqrt{gZ^3} / 3$. The value of the latter is obtained from the best fit of the experimental profile with the solution of Eq. (4). In order to obtain accurate measurements the experiments are performed in the case $u_0 \ll U$ for which most of the viscosity-limited stretching is observed and care is taken to verify the slenderness criterion ($Z \gg h_0$).

In addition to the extensional measurements, the shear effective viscosity of the suspensions is measured with a shear cell sketched in Fig. 1(b) which enables large values of the shear gap and is calibrated with Newtonian liquids (see details in [13,16]). The shear viscosity is found to be almost independent of the gap (less than 5% variation when the gap size is increased from 2.5 to 5 mm) and a slight shear thinning is observed for the largest solid fractions (typically, a 30% decrease over one decade of shear rate for $\phi = 0.20$ with $a = 11$). Therefore, we report the average as well as the extreme values measured over the shear rate decade $1\text{--}10 \text{ s}^{-1}$ which corresponds to the typical deformation rate u_z in the jet.

The breakup dynamics is studied with the capillary bridge apparatus sketched in Fig. 1(c). The setup is identical to that used in [17]. It consists in letting a static pending suspension drop with a controlled size to merge with a bath of the same suspension and monitoring the thinning and pinching of the unstable bridge that is transiently formed by the coalescence. The drop is quasistatically extruded from a stainless steel cylindrical nozzle with an outer diameter of 4.39 mm until its bottom is located 3.88 mm below the nozzle outlet. The suspension bath is then slowly raised (at typically $1 \mu\text{m/s}$) until the merging is triggered. The pinching dynamics of the bridge is imaged from a side view with a camera. The contour of the bridge is extracted and the time evolution of the minimal diameter of the bridge, h_{\min} , is followed from $h_{\min} = h_{\text{ref}} \equiv 2.5 \text{ mm}$ to the instant of the breakup, when h_{\min} vanishes. The experiments are conducted with the smallest fibers ($a = 10.8 \pm 1.8$, $d = 28.9 \pm 1.2 \mu\text{m}$) and for volume fractions, ϕ , ranging from 0.015 to 0.24. The suspending liquid viscosity ($\eta_0 = 0.13$ or 3.05 Pa s ; see Table III discussed in Sec. III) is chosen so as to obtain sufficiently large Ohnesorge numbers ($\eta_e / \sqrt{\rho h_{\text{ref}} \sigma} \gtrsim 10$, where $\sigma \simeq 38$ or 42 mPa/m , respectively, is the surface tension of the suspending liquid), which ensures that inertia does not affect the pinching. The typical deformation rates, $h_{\min} / h_{\min} \sim 10^{-1}$ to 1 s^{-1} , are slightly smaller than those in the jet ($u_z \sim 1$ to 10 s^{-1}). The viscous Newtonian reference dynamics is calibrated with the most viscous suspending liquid in the absence of particles. This ensures that the calibration is obtained for a surface tension that is within 10% that of the suspensions and a density that is equal.

For this range of parameters the Sperm number, $(128\eta_0\dot{\epsilon}/E)a^4 / \ln 2a$, which determines whether the magnitude of the viscous stresses is sufficient to bend an isolated fiber [18] (with $\dot{\epsilon} = u_z$ or \dot{h}_{\min}/h_{\min} the typical deformation rate and $E \approx 3\text{--}5 \text{ GPa}$ the Young modulus of the fibers), varies from $\sim 10^{-3}$ to ~ 10 (for a ranging from 11 to 103). This is below the critical value for buckling ≈ 150 [18]. It should be stressed that this criterion is relevant only for isolated fibers that are aligned with a compressive direction of the flow, i.e., that are close to perpendicular to the thread axis.

III. RESULTS

A. Jets

Figure 2(a) shows the typical jet profiles observed for a suspension of fibers with $a = 10.8 \pm 1.8$ and $d = 28.9 \pm 1.2 \mu\text{m}$ for both a dilute (left, $\phi = 0.01$) and a concentrated (right, $\phi = 0.20$) situation. In both cases, below a certain distance from the nozzle at which unsteady diameter modulations akin to a Plateau-Rayleigh instability eventually develop, an extended portion is observed where the jet is quasisteady. Over this portion, which is a few nozzle diameters long, the jet stretches and thins monotonically with increasing distance from the nozzle and the quasisteady thickness profile can be extracted. Figure 2(b) presents the stretching of the jet measured for the same fibers ($a = 10.8 \pm 1.8$, $d = 28.9 \pm 1.2 \mu\text{m}$) and a few representative values of ϕ between 0.01 and 0.22. All the velocity profiles (obtained using $u = u_0 h_0^2 / h^2$; see Sec. II) are found to show the quadratic law $u/U \propto (z/Z)^2$ of the viscosity-limited stretching regime ($u \ll U$) and to be well

TABLE II. Extensional effective viscosities obtained with the jet setup.

$a = l/d$	$a_{\text{eff}} = \sqrt{\frac{\langle l^3 \rangle}{\langle d^2 \rangle}}$	d (μm)	$\phi/100$	η_0 (Pa s)	η_e/η_0
10.8	11.2	28.9	1	3.10	1.35
			2.5	3.10	1.90
			5	3.10	2.77
			7.5	3.10	3.77
			10	0.66	6.1
			12.5	0.66	9.1
			15	0.60	11.8
			17.5	0.66	18.2
			20	0.66	36
			22	0.66	39
27.6	27.7	28.3	0.3	3.10	1.61
			1.3	3.10	3.16
			7	0.62	16.9
106	106	28.1	0.08	3.10	2.90
			0.4	3.10	6.13
			2	0.62	35.5
11.5	11.4	48.1	5	3.10	2.97

fitted by Eq. (4) (solid black line) over a significant range of strain, $h_0^2/h^2 \gg 10$. This suggests that the suspensions behave as an effective Newtonian liquid and that an extensional effective viscosity, η_e , can be measured.

The value of η_e relative to the suspending liquid viscosity, η_0 , is plotted as a function of the particle volume fraction in Fig. 2(c). It is found to increase strongly and continuously with increasing ϕ , reaching typically 40 at $\phi = 0.22$. In order to appreciate the influence of the particle size, Fig. 2(c) also reports the extensional viscosity measured for $\phi = 0.05$ for particles that have a similar shape ($a \approx 11$) but are almost twice as large ($d = 48.1 \pm 4.2 \mu\text{m}$ instead of $28.9 \pm 1.2 \mu\text{m}$). Within the experimental uncertainty, the same value of η_e/η_0 is obtained (2.97 for $d = 48.1 \pm 4.2$, vs 2.77 for $28.9 \pm 1.2 \mu\text{m}$), which suggests that our rheological measurements are not influenced by finite size effects and probe the bulk rheology of the suspensions.

The extensional viscosity of the suspension obtained with the jet experiment, η_e , can be compared to the shear effective viscosity, η_s , measured with the shear cell. As shown in Fig. 2(c), η_e remains larger than η_s over the whole range of ϕ . More specifically, the increase in η_e is found to be much larger than in η_s for the smallest volume fractions ($\phi \lesssim 0.08$), whereas for higher values of ϕ the two viscosities remain almost in the same ratio of approximately 4. This suggests that, as expected in the dilute limit [9,19], the fibers are more aligned with the straining direction in the jet than in the shear flow.

The dependence of the extensional effective viscosity on the fiber aspect ratio, a , is studied by increasing the length of the fibers while keeping their diameter ($d \approx 28 \mu\text{m}$; see Table I) and the range of $a\phi$ ($0.1 \lesssim a\phi \lesssim 2$; see Table I) almost unchanged. These data are provided in Table II as a function of both a and ϕ . Figure 3(a) compares these measurements with the prediction for the dilute regime, by representing the specific effective viscosity, $\eta_e/\eta_0 - 1$, as a function of the diluteness parameter, $\varepsilon Q(\varepsilon)a^2\phi$. For the smallest aspect ratio already discussed above ($a = 10.8 \pm 1.8$), $\eta_e/\eta_0 - 1$ is found to increase close to linearly with ϕ up to $\phi \approx 0.08$. This suggests that particle interactions have a negligible influence over this range of ϕ . This is also the case for the more slender fibers ($a = 27.6 \pm 0.9$ and 106 ± 5.5), albeit over the whole range of volume fraction investigated. In the $\eta_e/\eta_0 - 1$ vs $\varepsilon Q(\varepsilon)a^2\phi$ representation, all these measurements collapse onto the same line. They also collapse with the data previously obtained experimentally

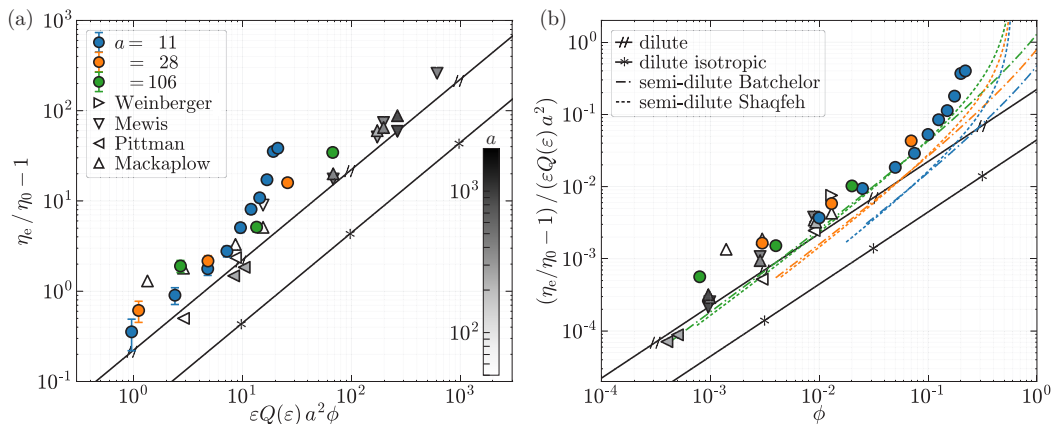


FIG. 3. (a) Specific extensional effective viscosity as a function of the diluteness parameter, $\varepsilon Q(\varepsilon) a^2 \phi$. The circles represent the values obtained with the jet setup for different aspect ratios but a similar particle diameter ($d \approx 28 \mu\text{m}$). The triangles represent the experimental data by Weinberger [7], Mewis and Metzner [6], Pittman and Bayram [8], and the numerical data by Mackaplow and Shaqfeh [20] (the value of a is given by the symbol darkness as indicated in the scale bar). The solid lines show the predictions for the dilute regime with aligned, Eq. (1), and isotropic fibers (see text in Sec. I). (b) Same viscosity as in (a) normalized by $\varepsilon Q(\varepsilon) a^2$ as a function of ϕ . The dash-dotted and dotted lines are the predictions for the semidilute regime, Eqs. (2a) and (2b), at the same aspect ratios as in the experiments.

(by Weinberger [7], Mewis and Metzner [6], and Pittman and Bayram [8]) and from numerical simulation (by Mackaplow and Shaqfeh [20]) for suspensions of thin and elongated fibers at lower volume fractions ($d \lesssim 10 \mu\text{m}$, $a \sim 50\text{--}1200$, and $\phi \sim 5 \times 10^{-4}$ to 0.01). All these measurements are found to agree, in trend and within a factor 2, with the dilute regime prediction of Batchelor, Eq. (1), assuming that the fibers do not interact and are aligned with the jet axis [21].

By contrast, the values measured at high volume fractions ($\phi \gtrsim 0.08$) for $a = 10.8 \pm 1.8$ are found to deviate from the dilute regime prediction and to increase much more strongly than linearly with ϕ . This deviation occurs for values of $\varepsilon Q(\varepsilon) a^2 \phi$ typically above 10, for which the viscosity for the more slender fibers is still following the dilute regime prediction. This indicates that the nonlinearity with volume fraction is not controlled by $a^2 \phi$ only (or even less by $a\phi$). The departure from linearity is more evidenced in Fig. 3(b) by plotting the specific effective viscosity normalized by $\varepsilon Q(\varepsilon) a^2$ as a function of ϕ . The semidilute models assuming sole hydrodynamics interactions, Eqs. (2a) and (2b), are predicting a much weaker deviation from linearity than that observed in the experiment and thus both fail to capture the experimental behavior at large ϕ .

B. Capillary breakup

We now turn to the capillary bridge experiments, with the aim of comparing the dynamics of pinching with that of jet stretching. Figures 4(b) and 4(c) show the typical time evolution of the capillary thinning observed for a suspension with $\phi = 0.05$ and 0.24, respectively, using the smallest fibers ($a = 10.8 \pm 1.8$, $d = 28.9 \pm 1.2 \mu\text{m}$). As a reference, the dynamics in the absence of fibers ($\phi = 0$) is also presented in panel (a). In the three cases, the bridge is shown for the same values of its minimal diameter ($h_{\min} = 2.5, 1, 0.5$, and 0.1 mm) and the corresponding times to breakup are indicated in the images (note that the suspending liquid is ≈ 23 times less viscous for $\phi = 0.24$ than for $\phi = 0$ and 0.05). For $\phi = 0.05$, the bridge shape is found to remain similar to that of the Newtonian case until the neck has decreased to a few fiber widths. By contrast, for $\phi = 0.24$, the bridge is found to be distorted at all times, showing a nonaxisymmetric shape with irregular protrusion, even when $h_{\min} \gg l$ ($\approx 290 \mu\text{m}$). As illustrated in Fig. 4(d), this irregularity in the shape

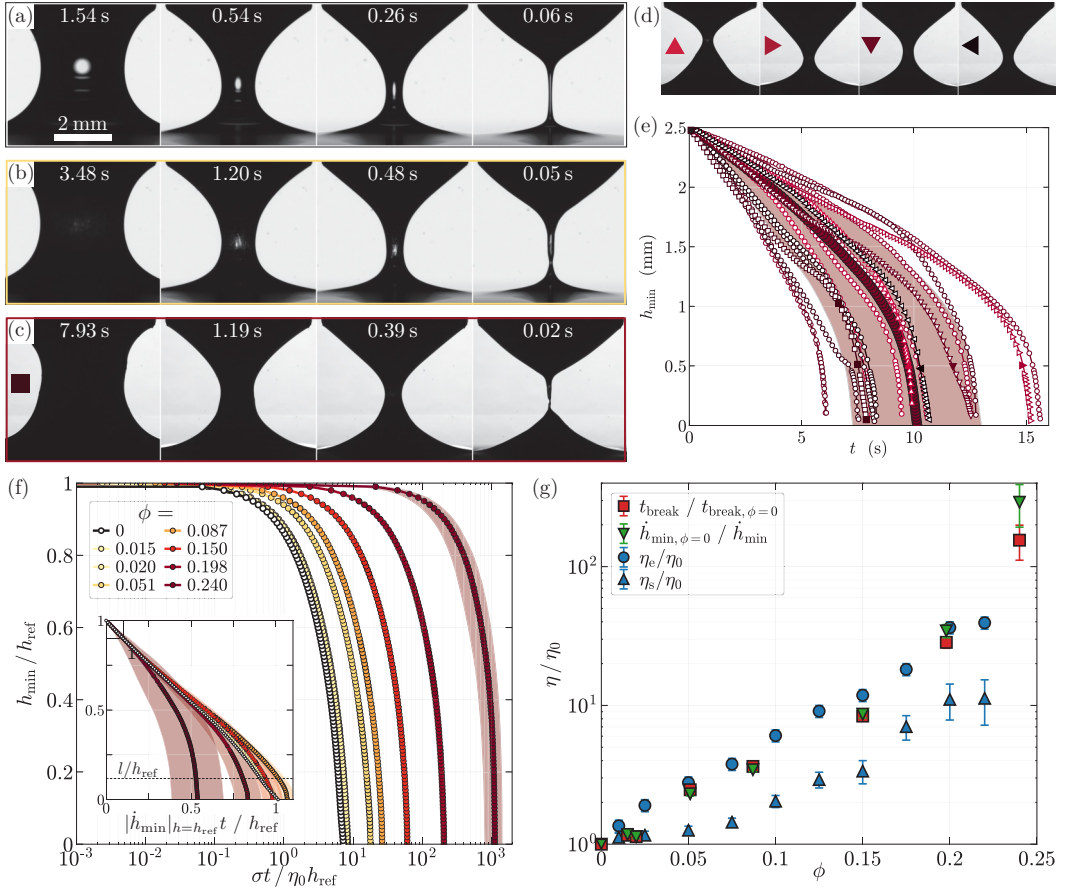


FIG. 4. (a)–(c) Typical breakup dynamics of the capillary bridge. From top to bottom, $\phi = 0, 0.05$, and 0.24 ($a = 10.8 \pm 1.8$, $d = 28.9 \pm 1.2 \mu\text{m}$, $\eta_0 = 3.05$ Pa s [for (a) and (b)] and 0.13 Pa s [for (c)]). The tags indicate the time, $t_{\text{break}} - t$, remaining before breakup (from left to right, $h_{\text{min}} = 2.5, 1, 0.5$, and 0.1 mm, respectively). (d) Variability in the bridge shape for four different breakup events with $\phi = 0.24$ ($h_{\text{min}} \approx 0.5$ mm). (e) Time evolution of the minimal diameter for 16 repetitions of the experiment with $\phi = 0.24$ (the time origin is taken when $h_{\text{min}} = h_{\text{ref}} = 2.5$ mm). The large filled symbols and the envelope show, respectively, the average and the standard deviation of t at a given value of h_{min} . The small filled symbols correspond to the images shown in (c) and (d). (f) Time evolution of the bridge minimal diameter for different particle volume fractions [average and standard deviation over 16 repetitions of the breakup, same value of a and d as in (a)–(d)]. Inset: Same data as a function of the time made dimensionless with the initial thinning rate $|\dot{h}_{\text{min}}|_{h_{\text{min}}=h_{\text{ref}}}/h_{\text{ref}}$ (the rate is measured between $h_{\text{min}} = h_{\text{ref}}$ and $h_{\text{min}} = 0.9h_{\text{ref}}$). (g) Relative thinning rate as inferred from the mean breakup time t_{break} and from the mean initial thinning rate $|\dot{h}_{\text{min}}|_{h_{\text{min}}=h_{\text{ref}}}/h_{\text{ref}}$ [same data for η_e/η_0 and η_s/η_0 as in Fig. 2(a)].

at high volume fraction ($\phi = 0.24$) is not deterministic. The bridge shape observed for the same value of h_{min} ($= 0.5$ mm) for four realizations of the experiment under the same conditions is found to differ strongly between each realization. This large variability in the shape results in a large variability in the temporal dynamics. Figure 4(e) compares the time evolution of h_{min} from the same reference diameter, $h_{\text{min}} = h_{\text{ref}} = 2.5$ mm, to the pinch-off instant ($h_{\text{min}} = 0$) for 16 breakup events. Both the whole duration of the breakup, which varies over a factor close to 3, and the shape of the thinning curve show a large variability around the average dynamics indicated by the large symbols.

TABLE III. Extensional effective viscosities obtained with the capillary bridge setup ($a = 10.8 \pm 1.8$, $d = 28.9 \pm 1.2 \mu\text{m}$). The values for the breakup time and initial thinning rate are averaged over 16 measurements and the value after the \pm symbol indicates the standard deviation.

$\phi/100$	η_0 (Pa s)	$t_{\text{break}}/t_{\text{break},\phi=0}$	$\dot{h}_{\text{min},\phi=0}/\dot{h}_{\text{min}}$
1.5	3.05	1.16 ± 0.03	1.18 ± 0.03
2	3.05	1.13 ± 0.04	1.13 ± 0.04
5.1	3.05	2.47 ± 0.14	2.31 ± 0.09
8.7	3.05	3.63 ± 0.15	3.44 ± 0.10
15	3.05	8.4 ± 0.5	8.7 ± 0.6
19.8	3.05	28.5 ± 2.7	34.5 ± 3.8
24	0.13	155 ± 44	291 ± 99

The influence of the particle volume fraction is summarized in Fig. 4(f), which compares the thinning dynamics obtained for ϕ ranging from 0 (Newtonian reference case) to 0.24. In the inset the time is nondimensionalized with the averaged initial thinning rate, $\dot{h}_{\text{min}}|_{h_{\text{min}}=h_{\text{ref}}}$, estimated around $h_{\text{min}} = h_{\text{ref}}$. This scale emphasizes the influence of the particle volume fraction on the variability of the dynamics. Relative to the mean time (symbols), the standard deviation of t at a given value of h_{min} (shaded envelop) increases continuously with increasing ϕ . The inset in Fig. 4(f) also evidences that the shape of the thinning law is ϕ -dependent. The larger the volume fraction becomes the more the thinning rate increases with decreasing h_{min} . This relative acceleration is qualitatively similar to the behavior observed for spherical particles [13,17,22–24]. However, its interpretation in the present case is much more delicate because for a suspension of fibers at high ϕ even the initial shape of the bridge (for $h_{\text{min}} \gtrsim h_{\text{ref}}$) is found to be influenced by the particles, hence preventing direct comparisons.

Besides these differences in the shape of the thinning law, the most conspicuous influence of the fibers is to slow down the pinching dynamics. As shown in the main graph of Fig. 4(f), where time is made dimensionless by using the typical pinching duration for $\phi = 0$, $\eta_0 h_{\text{ref}}/\sigma$, the whole pinching duration increases continuously with increasing ϕ and is found to be typically 10^2 times longer at $\phi = 0.24$ than at $\phi = 0$. The magnitude of this slowing of the dynamics is compared to the relative viscosity determined with the jet experiments in Fig. 4(g), where both the relative breakup time, $t_{\text{break}}/t_{\text{break},\phi=0}$, and the inverse of the relative initial thinning rate, $\dot{h}_{\text{min},\phi=0}/\dot{h}_{\text{min}}$, are reported as a function of ϕ . These data are also provided in Table III. These ratios are found to reflect quantitatively the extensional effective viscosity of the suspension, up to the largest volume fraction at which the two experiments can be compared ($\phi = 0.20$). This indicates that, in spite of the nonuniformity of the flow and of the differences with a Newtonian effective dynamics that have been mentioned above, the timescale of the pinching is well captured by the extensional bulk effective viscosity.

IV. CONCLUSIONS

Our measurements of the extensional bulk effective viscosity for moderate aspect ratios of the fibers and relatively high volume fractions ($a \sim 10$ to 10^2 and ϕ up to 0.24) complement those already available in the literature for more dilute suspensions of more slender fibers ($a \sim 10^2$ to 10^3 , $\phi \sim 10^{-4}$ to 10^{-2} [6–8]). Except for the most concentrated suspensions ($\phi \gtrsim 0.08$, $a \approx 11$), all the measurements are close to the dilute regime prediction assuming noninteracting fibers aligned with the strain direction. By contrast, for those most concentrated suspensions the specific viscosity, $\eta_e/\eta_0 - 1$, increases nonlinearly with ϕ and much more strongly than predicted by the semidilute models assuming purely hydrodynamic long distance interactions. This suggests that lubrication, contact interactions between the fibers, or intrinsic nonuniformities in the distribution of the fibers need to be considered in this concentrated regime.

Observation on the thinning of a capillary bridge (for $a \approx 11$) reveals a significant departure from the Newtonian effective dynamics at solid volume fractions ~ 0.20 that are significantly lower than the critical volume fraction reported in a pure shear flow, ~ 0.45 [12], or the random packing volume fraction reported for dry fibers, ~ 0.40 [25]. This departure manifests in less slender bridge shapes and in an acceleration of the thinning rate during the pinch-off ($|\dot{h}_{\min}| > 0$). For the most concentrated suspensions, the departure is observed even when the size of the flow is still much larger than the fiber length ($h_{\min}/l \gtrsim 10$), and is characterized by an important random feature producing a large variability in the shape of the bridge and in its temporal thinning law. However, in spite of these variabilities and of the nonuniformity and significant tridimensionality of the flow in the bridge, the total duration of the pinching is found to be in good quantitative agreement with the duration expected from a Newtonian effective dynamics limited by the extensional viscosity, η_e .

-
- [1] G. Batchelor, The stress generated in a non-dilute suspension, *J. Fluid Mech.* **46**, 813 (1971).
 - [2] E. Shaqfeh and G. Fredrickson, The hydrodynamic stress in a suspension of rods, *Phys. Fluids A* **2**, 7 (1990).
 - [3] G. Batchelor, Slender-body theory for particles of arbitrary cross-section in Stokes flow, *J. Fluid Mech.* **44**, 419 (1970).
 - [4] J. M. Burgers, On the motion of small particles of elongated form suspended in a viscous liquid. Chap. III of Second Report of Viscosity and Plasticity, Kon. Ned. Akad. Wet., Verhand. (Eerste Sectie) **16**, 113 (1938).
 - [5] R. Cox, The motion of long slender bodies in a viscous fluid. Part 1. General theory, *J. Fluid Mech.* **44**, 791 (1970).
 - [6] J. Mewis and A. Metzner, The rheological properties, *J. Fluid Mech.* **62**, 593 (1974).
 - [7] C. Weinberger and J. Goddard, Extensional flow behavior of polymer solutions and particle suspensions in a spinning motion, *Int. J. Multiph. Flow* **1**, 465 (1974).
 - [8] J. Pittman and J. Bayram, Extensional flow of polydisperse fiber suspensions in free-falling liquid jets, *Int. J. Multiph. Flow* **16**, 545 (1990).
 - [9] J. Butler and B. Snook, Microstructural dynamics and rheology of suspensions of rigid fibers, *Annu. Rev. Fluid Mech.* **50**, 299 (2018).
 - [10] C. Petrie, The rheology of fibre suspensions, *J. Non-Newt. Fluid Mech.* **87**, 369 (1999).
 - [11] R. Powell, Rheology of suspensions of rodlike particles, *J. Stat. Phys.* **62**, 1073 (1991).
 - [12] F. Tapia, S. Shaikh, J. E. Butler, O. Pouliquen, and É. Guazzelli, Rheology of concentrated suspensions of non-colloidal rigid fibres, *J. Fluid Mech.* **827**, 725 (2017).
 - [13] J. Château and H. Lhuissier, Breakup of a particulate suspension jet, *Phys. Rev. Fluids* **4**, 012001(R) (2019).
 - [14] F. T. Trouton, On the coefficient of viscous traction and its relation to that of viscosity, *Proc. R. Soc. Lond. A* **77**, 426 (1906).
 - [15] D. Brown, A study of the behavior of a thin sheet of moving liquid, *J. Fluid Mech.* **10**, 297 (1961).
 - [16] S. Palma and H. Lhuissier, Dip-coating with a particulate suspension, *J. Fluid Mech.* **869**, R3 (2019).
 - [17] J. Château, É. Guazzelli, and H. Lhuissier, Pinch-off of a viscous suspension thread, *J. Fluid Mech.* **852**, 178 (2018).
 - [18] Y. Young and M. Shelley, Stretch-Coil Transition and Transport of Fibers in Cellular Flows, *Phys. Rev. Lett.* **99**, 058303 (2007).
 - [19] G. B. Jeffery, The motion of ellipsoidal particles immersed in a viscous fluid, *Proc. R. Soc. Lond. A* **102**, 161 (1922).
 - [20] M. Mackaplow and E. Shaqfeh, A numerical study of the rheological properties of suspensions of rigid, non-Brownian fibres, *J. Fluid Mech.* **329**, 155 (1996).
 - [21] Note that the difference between the experimental values and the dilute regime prediction cannot be attributed to the dispersion in the fiber dimensions. As shown in Table II, the effective value of the

aspect ratio, $a_{\text{eff}} = \sqrt{\langle l^3 \rangle / \langle l d^2 \rangle}$, obtained by weighting each fiber proportionally to its contribution to the increase in viscosity in Eq. (1), is very close to the simple average of $a = l/d$ used for the comparisons in Fig. 3.

- [22] C. Bonnoit, T. Bertrand, E. Clément, and A. Lindner, Accelerated drop detachment in granular suspensions, *Phys. Fluids* **24**, 043304 (2012).
- [23] R. J. Furbank and J. F. Morris, An experimental study of particle effects on drop formation, *Phys. Fluids* **16**, 1777 (2004).
- [24] W. Mathues, C. McIlroy, O. G. Harlen, and C. Clasen, Capillary breakup of suspensions near pinch-off, *Phys. Fluids* **27**, 093301 (2015).
- [25] O. Rahli, L. Tadrist, and R. Blanc, Experimental analysis of the porosity of randomly packed rigid fibers, *C. R. Acad. Sci., Ser. Iib* **327**, 725 (1999).